Received: 22 September 2023 | Revised: 4 July 2024 | Accepted: 18 August 2024

DOI: 10.1002/mop.34309

RESEARCH ARTICLE

WILEY

A miniaturized on-chip BPF with low insertion loss and wide stopband based on integrated passive device technology

Fuwang Li | **Yi-Feng Cheng** | **Gaofeng Wang**

School of Electronics and Information Engineering, Hangzhou Dianzi University, Hangzhou, China

Correspondence
Yi-Feng Cheng, School of Electronics and Information Engineering, Hangzhou Dianzi University, 310018 Hangzhou, China.
Email: chengyifeng2013@gmail.com

Funding information
National Natural Science Foundation of China, Grant/Award Numbers: 62201183, 62141409, 92373202; Wenzhou Basic Industrial Project, Grant/Award Number: G20240045; Natural Science Foundation of Zhejiang Province, Grant/Award Number: LY22F010020; Laboratory of Flexible Electronics Technology, Tsinghua University

Abstract

In this study, a novel bandpass filter (BPF) characterized by low insertion loss (IL) and the presence of two transmission zeros (TZs) based on integrated passive device (IPD) technology is introduced. The design incorporates a low-pass filter and a high-pass filter which both exhibit strong out-of-band suppression performance. The control structure for TZs is constructed by cascading the inductance and capacitance components. The TZ controlling structure primarily generates TZs at high frequencies, resulting in a further bandwidth enhancement in the stopband. The lumped circuit of the proposed BPF is first constructed, and rigorous design formulas are provided to assist in constructing the proposed design. After schematic optimization, the second step involves layout optimization and simulation based on the specific IPD process. Experimental results mounted on a printed circuit board demonstrate that the bandwidth spans from 3.3 to 4.2 GHz with an IL of only 2.0 dB at the center frequency. Additionally, this BPF achieves impressive sideband suppression, exceeding 18 dB in the 0–1.7 GHz range and 30 dB in the 9–15 GHz range. Remarkably, the BPF is exceptionally compact with only 0.5 mm × 1.0 mm ($0.006\lambda_c \times 0.012\lambda_c$). The proposed BPF exhibits outstanding performance with minimal IL and extensive sideband suppression at such a compact size based on the IPD technology.

KEYWORDS

bandpass filter, integrated passive device, low insertion loss, TZ control structure, wide stopband

1 | INTRODUCTION

The utilization of on-chip bandpass filters (BPFs) based on integrated passive device (IPD) technology has become increasingly prevalent in 5G mobile phone RF front-ends. This popularity is attributed to their exceptional performance characteristics, including compact size, seamless integration, cost-effectiveness, consistency, and enhanced reliability. The primary benchmarks for evaluating BPF performance encompass wide sideband suppression and low insertion loss (IL), as they directly impact the filter's ability to mitigate undesired frequency components and minimize energy loss within the passband.[1] In pursuit of achieving an extensive operating bandwidth with minimal IL, coupled with impressive impedance matching capabilities characterized by high return loss, and a broad stopband featuring sharp skirt characteristics, numerous techniques[2–11] have emerged

in recent years. For instance, Luo et al.[2] proposed an on-chip BPF with remarkable features, including an ultra-wide stopband, high selectivity, and IL of less than 2.5 dB in the passband. Achieving high sideband suppression (>30 dB) is accomplished through source–load coupling between input and output ports, along with the inclusion of a Pi-section circuit at the output ports. In Yang et al.,[3] the out-of-band attenuation of a proposed Marchand balun-based BPF is enhanced by increasing the order of the Chebyshev low-pass filter. Wu et al.[4] utilize a combination of low- and high-pass filters to create cascades that improve out-of-band rejection (>30 dB) and yield an ultrawideband BPF using silicon-based IPD technology. Both Lee et al.[5] and Machavaram et al.[6] employ a conversion method from simple circuit-level elements to layout-level structures for designing BPFs based on Si-based IPD technology. Jiang et al.[7] achieve an ultra-wideband upper stopband with a sharp roll-off performance by introducing a π-section circuit structure based on GaAs IPD Technology. In Bautista et al.,[8] a quasilumped elements technique is introduced to attain high stopband attenuation (over 20 dB) from DC to 20.5 GHz and from 48 to 67 GHz, respectively. Yang et al.[9] employ grounded center-tapped ring resonator methods to achieve two transmission poles and good stopband rejection (>20 dB) beyond 58 GHz. Li et al.[10] realize two transmission zeros (TZs) on both sides of the passband by placing a capacitor inside the octagon inductor. Lastly, Zhao et al.[11] introduce the equivalent circuit (EC) of the BPF filter and the design process for band rejection, resulting in a BPF with low IL and high out-of-band suppression. However, it is worth noting that the methods mentioned above, while effective, have certain limitations, such as narrow stopband bandwidth, narrow operating bandwidth, and high IL. In Khani et al.,[12,13] Kiani et al.,[14] and Hao et al.,[15] the proposed filters manufactured using the general printed circuit board (PCB) and LTCC technology have low IL; however, their large size is not suitable for the highly integrated and miniaturized design of current modern RF systems. Similarly, filters in Ge et al.,[16] Liu et al.,[17] and Xu and Liu,[18] designed for millimeter-wave bands with center frequencies of 34.5, 70.65, and 67 GHz, respectively, display increased IL and greater dimensions.

This paper presents a novel BPF characterized by low IL, high return loss, and a wide stopband. It achieves good out-of-band suppression at both high and low frequencies, resulting in sideband suppression of over 18 dB from 0 to 1.7 GHz and over 30 dB from 9 to 15 GHz, while maintaining an operating bandwidth of 3.3-4.2 GHz. The BPF incorporates a TZ control structure to enhance its selectivity, which is both simple and compact, and its impact on antenna selectivity is investigated. Additionally, rigorous design formulas are provided to assist in the design process. Experimental results confirm that this proposed BPF exhibits low IL, high return loss, and a wide stopband as a promising choice for modern wireless communication systems.

2 | PROPOSED DESIGN

2.1 | Lumped structure of the proposed BPF

Figure 1A illustrates the EC of the proposed BPF, comprising one high-pass filter, one low-pass filter, and one zero control structure (ZCS). To attenuate the filter's response in the lower frequency range, a high-pass filter is employed to generate a low-frequency zero. This component consists of three capacitors and an inductor, forming the first part of the BPF. Similarly, to suppress the filter's response in the higher frequency range, a low-pass filter is utilized to generate a high-frequency zero. This part consists of two inductors and a capacitor, constituting the second portion of the BPF. However, a simple series of high- and low-pass filters alone fails to achieve the desired stopband rejection and bandwidth, particularly in the high-frequency range of 9–15 GHz. To address this limitation, a novel zero control circuit is introduced to primarily enhance the upper stopband

(A)

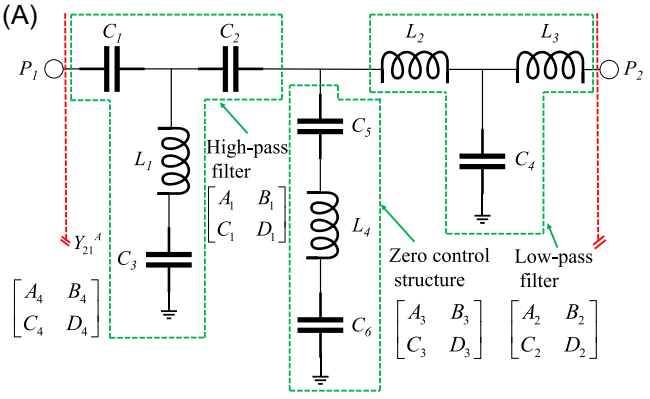

(B)

C_1	C_2	C_3	C_4	C_5
0.64nF	1.18nF	4.17nF	0.57nF	2.39nF
C_6	L_1	L_2	L_3	L_4
0.64nF	1.80nH	2.79nH	2.73nH	0.63nH

FIGURE 1 The proposed BPF. (A) Equivalent circuit based on lump elements and (B) specified lumped inductor and capacitance values with additional ZCS. BPF, bandpass filter; ZCS, zero control structure.

rejection. This circuit comprises an inductor and two capacitors cascaded between the high- and low-pass filters.

In Figure 2A, the BPF with an added ZCS is compared with the conventional lumped BPF without ZCS. This addition enhances the rejection of the existing TZ located in the upper stopband. Simultaneously, it exhibits slightly improved IL, return loss, and low-frequency stopband suppression. The values of inductance and capacitance are determined by the inner diameter, coil number of the inductor, and the parallel plate length of the capacitor. These values can be derived from their self-admittance using microwave admittance theory, as shown in Equations (1) and (2). The specific values of lumped inductors and capacitance at the center frequency of 3.75 GHz for the proposed BPF with the added ZCS are provided in Figure 1B.

$$L = im(1/Y(1,1))/(2\pi f), \tag{1}$$

$$C = im(Y(1,1))/(2\pi f). \tag{2}$$

To better understand the impact of the ZCS on the upper stopband zero, Figure 2B–D depicts the deviation of the TZ as the inductance L_4 and capacitance C_5 and C_6 within the ZCS vary independently. In Figure 2B, it is evident that as the inductance L_4 increases, the TZ in the upper stopband shifts towards lower frequencies. Similarly, as shown in Figure 2C,D, when capacitance C_5 and C_6 increase, respectively, the TZ in the upper stopband also moves to lower frequencies. These variations in the values of inductance L_4 and capacitance C_5 and C_6 have a minor impact on low-frequency stopband suppression.

2.2 | Suppression mechanism of ZCS

Refer to Figure 1, let $[A_1, B_1; C_1, D_1]$ and $[A_2, B_2; C_2, D_2]$ denote the transmission matrices (TMs) of high- and low-pass filters, respectively. The TM of the ZCS circuit is denoted by $[A_3, B_3; C_3, D_3]$, and the TM with respect to the ports 1 and 2 of the BPF is denoted by $[A_4, B_4; C_4, D_4]$. Applying two-port network theory in Cheng and Cheng[19–21] and Pozar,[22] the following equation can be derived:

$$\begin{bmatrix} A_1 & B_1 \\ C_1 & D_1 \end{bmatrix} = \begin{bmatrix} 1 & 1/jwC_1 \\ 0 & 1 \end{bmatrix} \begin{bmatrix} 1 & 0 \\ jwC_3/1 - w^2L_1C_3 & 1 \end{bmatrix} \cdot \begin{bmatrix} 1 & 1/jwC_1 \\ 0 & 1 \end{bmatrix}, \tag{3}$$

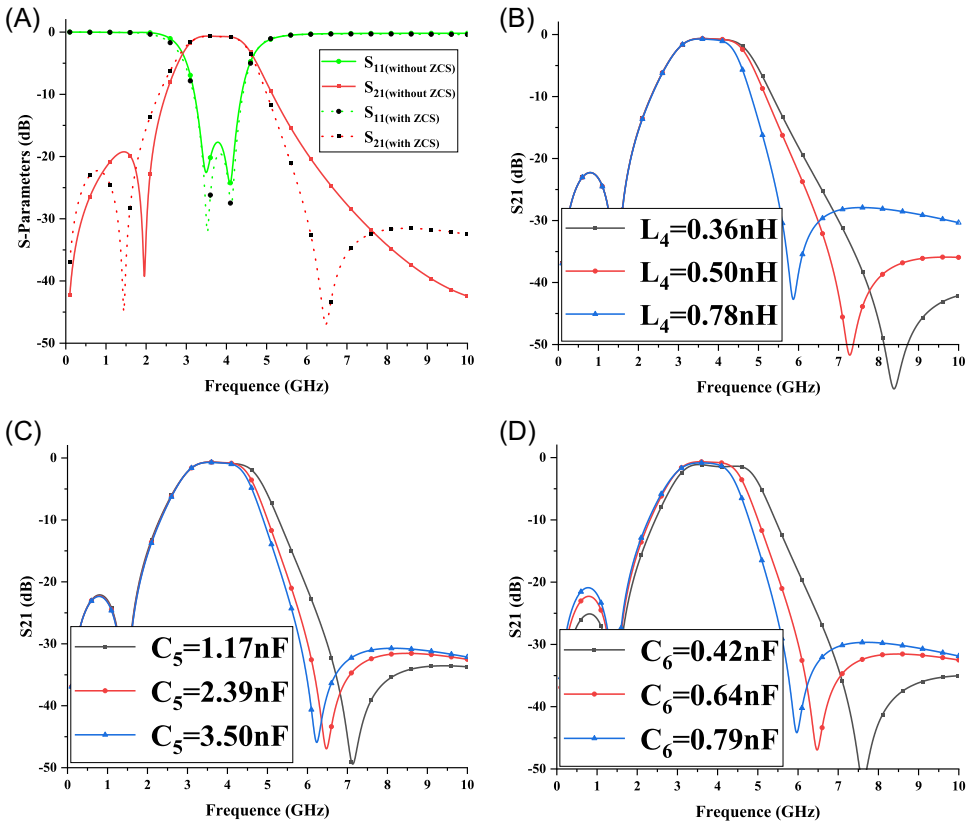

FIGURE 2 Impact for the TZ of the upper band. (A) With and without additional ZCS, (B) inductance value of L_4, (C) capacitance value of C_5, and (D) capacitance value of C_6. TZ, transmission zero; ZCS, zero control structure.

$$\begin{bmatrix} A_2 & B_2 \\ C_2 & D_2 \end{bmatrix} = \begin{bmatrix} 1 & jwL_2 \\ 0 & 1 \end{bmatrix} \begin{bmatrix} 1 & 0 \\ jwC_4 & 1 \end{bmatrix} \cdot \begin{bmatrix} 1 & jwL_3 \\ 0 & 1 \end{bmatrix}, \tag{4}$$

$$\begin{bmatrix} A_3 & B_3 \\ C_3 & D_3 \end{bmatrix} = \begin{bmatrix} 1 & 0 \\ \frac{jwC_5C_6}{C_5+C_6-w^2L_4C_5C_6} & 1 \end{bmatrix}, \tag{5}$$

$$\begin{bmatrix} A_4 & B_4 \\ C_4 & D_4 \end{bmatrix} = \begin{bmatrix} A_1 & B_1 \\ C_1 & D_1 \end{bmatrix} \begin{bmatrix} A_2 & B_2 \\ C_2 & D_2 \end{bmatrix} \cdot \begin{bmatrix} A_3 & B_3 \\ C_3 & D_3 \end{bmatrix}. \tag{6}$$

Subsequently, the mutual admittance with reference to the ports 1 and 2 of the BPF can be calculated as follows:

$$Y_{21}{}^{A} = -\frac{1}{B_4}, \tag{7}$$

$$Y_{21}{}^{A} = 0. \tag{8}$$

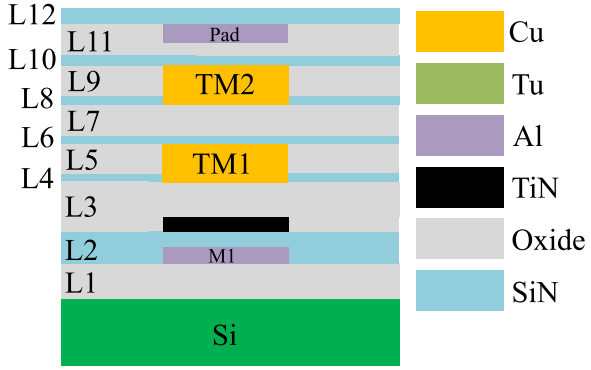

FIGURE 3 Cross-section view of the silicon-based IPD technology. IPD, integrated passive device; TM, transmission matrix.

To achieve TZ characteristic ($Y_{21} = 0$), Equation (8) should be satisfied at f_3. By adjusting the values of inductance L_4 and capacitance C_5 and C_6, the independently controlled TZ can be created at f_3, as shown in Figure 2.

2.3 | Silicon-based IPD process

A standard silicon-based IPD technology is employed for the proposed BPF. Figure 3 provides a cross-sectional view of silicon-based IPD technology, illustrating the positions and overlapping relationships between the metal and dielectric layers, which comprise a total of 12 dielectric layers. The sequence and thickness of the dielectric layers from bottom to top are as follows: 4, 0.7, 3.15, 0.1, 2.9, 0.1, 2.9, 0.1, 2.9, 0.4, 0.4, and 0.4 μm. The Si substrate layer at the bottom has a thickness of 725 μm. The dielectric constants and loss tangents for the oxide and SiN in the dielectric layers are 4 and 0.01, and 7 and 0.004, respectively. The metal aluminum is present in dielectric layers 2 (M1) and 11 (Pad), copper is present in dielectric layers 4 and 5 (TM1) and layers 8 and 9 (TM2), and titanium nitride (TiN) is in dielectric layer 3. The M1–TM1 configuration is used to construct a metal–insulator–metal (MIM) capacitor. M1 and TiN are connected to the metal layer TM1 through tungsten vias. TM2 is connected to the metal Pad through aluminum vias. And TM1 is connected to TM2 through copper vias.

It is important to note that the values of the proposed lumped circuit elements (in part A) are sourced from the electromagnetic (EM) simulation software Process Design Kit provided by the Foundry. However, in the actual layout, the proposed BPF utilizing silicon-based IPD technology experiences increased IL due to factors, such as higher dielectric loss, proximity effect, skin effect loss, and coupling effect loss.

Moreover, the parameters of the proposed filter well-optimized in the schematic diagram require reoptimization

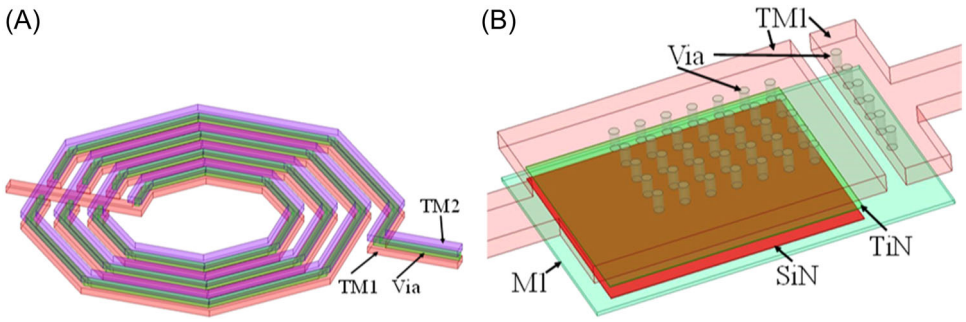

FIGURE 4 Three-dimensional view meeting DRC. (A) Regular octagon inductance and (B) MIM capacitance. DRC, design rules checks; MIM, metal–insulator–metal; TM, transmission matrix.

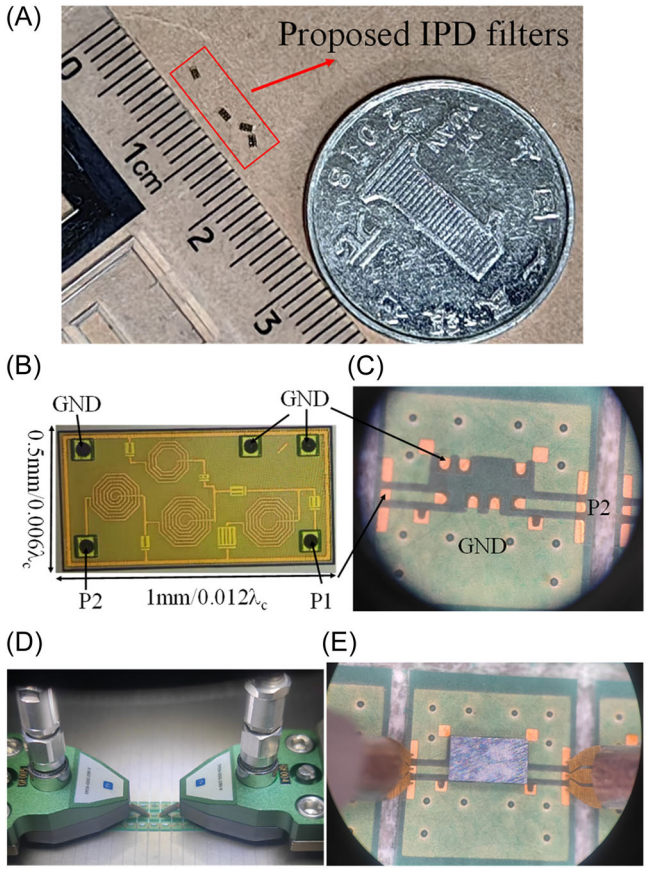

FIGURE 5 Photographs of proposed BPF. (A) A photo of four proposed IPD filters alongside a one-RMB coin, (B) a micrograph of the proposed circuit, (C) the testing PCB, (D) the probe station, and (E) the testing PCB with a proposed chip. BPF, bandpass filter; IPD, integrated passive device; PCB, printed circuit board.

in the layout. It is quite likely that the optimal results in the layout optimization may not match the optimal performance in the schematic diagram.

Figure 4A,B shows the 3D views of the standard octagonal inductor and MIM capacitor with clear figure, which can be fabricated to comply with design rules checks and process requirements using silicon-based IPD technology. It is important to highlight that employing more inductance layers and through holes in the MIM capacitor results in lower IL for the BPF.

3 | PACKAGE AND MEASUREMENT

There are two common chip testing methods: testing the bare chip and testing the chip together with a PCB. Testing the bare chip may yield better IL results, while testing the chip and PCB combination allows for practical use in various RF systems, forming a complete signal link.

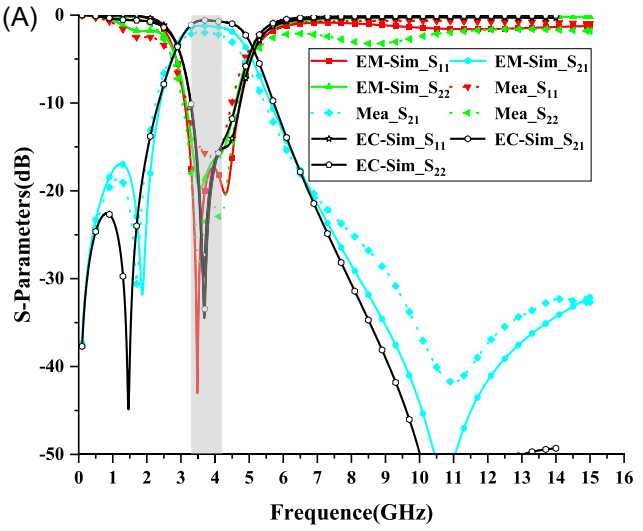

(B)

Ref.	Type: Sub	f_0(GHz)	Insertion Loss (dB)	Return Loss (dB)	Lower / Upper stopband	Size (λc^2)
[1]	SiO_2	33	2.6	10	$0.5/1.7f_0$	0.014×0.033
[2]	GaAs	3.35	2.05	10	$0.6/1.8f_0$	0.007×0.017
[3]	GaAs	4.04	5	10	$0.2/2.4f_0$	0.019×0.02
[7]	GaAs	3.75	1.8	11.7	$0.5/1.7f_0$	0.008×0.02
[13]	RT/Dourid 5880	2.4	0.64	N.A	$0.8/1.3f_0$	0.126×0.132
[14]	Rogers RO4003	10	0.8	N.A	$0.9/1.1f_0$	1.5×2.0
[15]	RT/Dourid 5880	3.6	0.45	N.A	$0.8/1.4f_0$	0.21×0.26
This work	**Si**	**3.75**	**2.0**	**14**	$\mathbf{0.3/2}f_0$	**0.006×0.012**

FIGURE 6 The proposed bandpass filter (BPF). (A) Equivalent circuit (EC), electromagnetic (EM) simulated, and measured *S*-parameters, and (B) comparisons with other published wide-stopband BPFs.

The proposed BPF based on silicon-based IPD technology has been fabricated and tested. Figure 5 shows the photographs of the BPF setup. Figure 5A shows a photo of four proposed IPD filters alongside a one-RMB coin. Figure 5B shows the top view of the bare chip with a tapered design, which fabricated filter is exceptionally compact with only 0.5 mm × 1.0 mm ($0.006\lambda_c \times 0.012\lambda_c$). Figure 5C shows the PCB used for testing and practical applications, situated beneath the chip. Figure 5D illustrates the probe station used for testing, and Figure 5E depicts the chip and PCB combined for probe testing, with the chip covering the PCB. The ground-source-ground ports of the probe are directly connected to the

PCB. *S*-parameter measurements were conducted using the Keysight PAN-X Network Analyzer N5247A. The *S*-parameters of EC, EM simulation, and measurement are compared in Figure 6A. Below, the EC, the EM simulation results, and the test results exhibit a close alignment. As depicted in Figure 6A, the measurement results confirm that the BPF meets the bandwidth requirements from 3.3 to 4.2 GHz, with an IL of 2.0 dB at 3.75 GHz. Moreover, it achieves more than 18 and 30 dB sideband suppression at 0–1.7 and 9–15 GHz, respectively. The BPF size is only 1 mm × 0.5 mm. The discrepancies between simulation and testing results may be attributed to factors such as machining precision, testing environment conditions, and losses incurred by the PCB board, indicating the potential for this filter's application in 5G mobile phone RF front-end systems.

In the BPF based on the IPD process proposed in this paper, a new benchmark is redefined to effectively characterize the roll-off performance. In this study, we opt for 20 dB as the reference point and document the corresponding frequency at the initial 20 dB drop on both sides of the BPF, transitioning from the pass band to the stop band.

Figure 6B provides comparisons of the BPF with other published wide-stopband BPFs. As shown in the table, there are four references [1–3, 7] for Chip-level filters and three references [12–14] for PCB-level filters. Chip-level filters are significantly smaller than PCB-level ones. Notably, PCB-level filters have lower IL due to its lower conductive loss. This proposed BPF achieve low IL, good return loss, wide stopband, and compact size.

4 | CONCLUSION

This paper presented a novel BPF designed using IPD technology achieving low IL and broad out-of-band suppression. One EC model of the proposed BPF was introduced to analyze the suppression mechanism of the ZCS. Additionally, the layout circuits for the proposed BPF were designed, simulated, and optimized using EM simulations. The measured results demonstrated over 18 and 30 dB sideband suppression at 0–1.7 and 9–15 GHz, respectively. The proposed BPF can achieve the low IL, good return loss, wide stopband, and compact size.

ACKNOWLEDGMENTS

The authors would like to thank Faraday Dynamics Ltd.[23] for providing useful simulation software (UltraEM V2022) to assist the research in this paper. This work was supported by the National Natural Science Foundation of China under Grants 62201183, 92373202, and 62141409; Wenzhou Basic Industrial Project G20240045; Natural Science Foundation of Zhejiang Province LY22F010020; and Laboratory of Flexible Electronics Technology, Tsinghua University.

DATA AVAILABILITY STATEMENT

Data sharing is not applicable to this article as no new data were created or analyzed in this study.

ORCID

Yi-Feng Cheng http://orcid.org/0000-0002-2364-0372
Gaofeng Wang http://orcid.org/0000-0001-8599-7249

REFERENCES

1. Zhong Y, Yang Y, Zhu X, Dutkiewicz E, Shum KM, Xue Q. An on-chip bandpass filter using a broadside-coupled meander line resonator with a defected-ground structure. *IEEE Electron Device Lett*. 2017;38(5):626-629.
2. Luo X-H, Cheng X, Zhang L, et al. A miniaturized on-chip BPF with ultrawide stopband based on lumped Pi-section and source–load coupling. *IEEE Microwave Wireless Compon Lett*. 2019;29(8):516-519.
3. Yang Y, Wu Y, Zhuang Z, Kong M, Wang W, Wang C. An ultraminiaturized bandpass filtering Marchand balun chip with spiral coupled lines based on GaAs integrated passive device technology. *IEEE Trans Plasma Sci*. 2020;48(9):3067-3075.
4. Wu Z, Shim Y, Rais-Zadeh M. Miniaturized UWB filters integrated with tunable notch filters using a silicon-based integrated passive device technology. *IEEE Trans Microwave Theory Tech*.2012;60(3):518-527.
5. Lee Y-T, Liu K, Frye R, Kim H-T, Kim G, Ahn B. Ultra-wideband (UWB) band-pass-filter using integrated passive device (IPD) technology for wireless applications. *2009 Electronic Components and Technology Conference, ECATC*; 2009:1994-1999.
6. Machavaram VR, Rao Nistala B. A high performance miniaturized onchip 25 GHz narrow bandpass filter for 5G radio access applications. *2019 International Conference and Workshops on Recent Advances and Innovations in Engineering, CRAIE*; 2019:1-5.
7. Jiang Y, Feng L, Zhu H, et al. Bandpass filter with ultra-wide upper stopband on GaAs IPD technology. *IEEE Trans Circuits Syst II*. 2022;69(2):389-393.
8. Bautista MG, Zhu H, Zhu X, Yang Y, Sun Y, Dutkiewicz E. Compact millimeter-wave bandpass filters using quasi-lumped elements in 0.13-μm (Bi)-CMOS technology for 5G wireless systems. *IEEE Trans Microwave Theory Tech*. 2019;67(7):3064-3073.
9. Yang Y, Liu H, Hou ZJ, Zhu X, Dutkiewicz E, Xue Q. Compact on-chip bandpass filter with improved in-band flatness and stopband attenuation in 0.13-μm (Bi)-CMOS technology. *IEEE Electron Device Lett*. 2017;38(10):1359-1362.
10. Li N, Li X-z, Xing M-J, Chen Q, Yang X-d. Design of super compact bandpass filter using silicon-based integrated passive device technology. *2017 International Conference on Electronic Packaging Technology, ICEPT*; 2017:1069-1072.
11. Zhao T, Cai J, Li Y, Wang Q, Wang D. Integrated passive filters based on silicon substrate for SiP application. *2013 IEEE Electronics Packaging Technology Conference, EPTC*; 2013:510-515.
12. Khani S, Makki SVA-D, Mousavi SMH, Danaie M, Rezaei P. Adjustable compact dual-band microstrip bandpass filter

using T-shaped resonators. *Microwave Opt Technol Lett.* 2017;59(12):2970-2975.
13. Khani S, Danaie M, Rezaei P, Shahzadi A. Compact ultra-wide upper stopband microstrip dual-band BPF using tapered and octagonal loop resonators. *Frequenz—Berlin*. 2019;74:1-2.
14. Kiani S, Rezaei P, Karami M, Sadeghzadeh RA. Substrate integrated waveguide quasi-elliptic bandpass filter with parallel coupled microstrip resonator. *Electron Lett*. 2018;54(10):667-668.
15. Hao L, Wu Y, Wang W, Yang Y. Design of on-chip dual-band bandpass filter using lumped elements in LTCC technology. *IEEE Trans Circuits Syst II*. 2022;69(3):959-963.
16. Ge Z, Chen L, Gómez-García R, Zhu X. Millimeter-wave wideband bandpass filter in CMOS technology using a two-layered highpass-type approach with embedded upper stopband. *IEEE Trans Circuits Syst II*. 2021;68(5):1586-1590.
17. Liu Y, Weng X, Xu K-D. Millimeter-wave bandpass filter based on spiral resonators and DGS using SiGe BiCMOS technology. *IEEE Trans Circuits Syst II*. 2023;70(7):2385-2389.
18. Xu K-D, Liu Y. Millimeter-wave on-chip bandpass filter using complementary-broadside-coupled structure. *IEEE Trans Circuits Syst II*. 2023;70(8):2829-2833.
19. Cheng Y-F, Cheng K-KM. A novel dual-band decoupling and matching technique for asymmetric antenna arrays. *IEEE Trans Microwave Theory Tech.*2008;56(5):2080-2089.
20. Cheng Y-F, Cheng K-KM. Decoupling of 2 × 2 MIMO antenna by using mixed radiation modes and novel patch element design. *IEEE Trans Antennas Propag*. 2021;69(12):8204-8213.
21. Cheng Y-F, Cheng K-KM. Novel wideband decoupling technique for MIMO antenna arrays with two independently controlled transmission zeros. *IEEE MTT-S Int Microwave Symp.*2017:853-856.
22. Pozar DM. *Microwave Engineering*; 2005.
23. Wang G. UltraEM V2022, Faraday Dynamics Inc.; 2022.

How to cite this article: Li F, Cheng Y-F, Wang G. A miniaturized on-chip BPF with low insertion loss and wide stopband based on integrated passive device technology. *Microw Opt Technol Lett*. 2024;66:e34309. doi:10.1002/mop.34309